Hybrid electrolyte with robust garnet-ceramic electrolyte for lithium anode protection in lithium-oxygen batteries

Jin Wang[1,2], Yanbin Yin[1,2], Tong Liu[1], Xiaoyang Yang[1,2], Zhiwen Chang[1,3], and Xinbo Zhang[1] (✉)

[1] *State Key Laboratory of Rare Earth Resource Utilization, Changchun Institute of Applied Chemistry, Chinese Academy of Sciences, Changchun 130022, China*
[2] *Key Laboratory of Automobile Materials, Ministry of Education and College of Materials Science and Engineering, Jilin University, Changchun 130012, China*
[3] *University of Chinese Academy of Sciences, Beijing 100049, China*

ABSTRACT

Rechargeable lithium-oxygen (Li-O$_2$) batteries have received intensive research interest due to its ultrahigh energy density, while its cycle stability is still hindered by the high reactivity of the Li anode with oxygen and moisture. To alleviate the corrosion of the metallic lithium anodes for achieving a stable Li-O$_2$ battery, and as a proof-of-concept experiment, a distinctive hybrid electrolyte system with an organic/ceramic/organic electrolyte (OCOE) architecture is designed. Importantly, the cycle number of Li-O$_2$ batteries with OCOE is significantly improved compared with batteries with an organic electrolyte (OE). This might be attributed to the effective suppression of the lithium anode corrosion caused by the OE degradation and the crossover of oxygen from the cathode. We consider that our facile, low-cost, and highly effective lithium protection strategy presents a new avenue to address the daunting corrosion problem of lithium metal anodes in Li-O$_2$ batteries. In addition, the proposed strategy can be easily extended to other metal-O$_2$ battery systems, such as Na-O$_2$ batteries.

1 Introduction

With the growing demand for electrical energy storage systems worldwide, Li-O$_2$ batteries, in recent years, have emerged as an appealing next-generation energy storage system because their theoretical energy density is nearly ten-times higher than that of state-of-art lithium-ion batteries [1, 2]. Although attractive, Li-O$_2$ battery technology is still in its infancy.

A typical Li-O$_2$ battery, composed of a cathode, electrolyte, and Li anode, has many urgent problems for each part that needs to be resolved. Among them is the serious corrosion of the Li anode, which is considered as the Achilles' heel of Li-O$_2$ batteries [3]. Firstly, while the battery is in operation, superoxide molecules (a discharge intermediate) and H$_2$O (a decomposition product of OE) corrodes the Li anode. Second, the Li anode reacts with the gaseous oxygen dissolved in the OE [4, 5]. Although the OE possesses high ionic conductivity, it not only suffers from serious decomposition, but it also cannot prevent the diffusion of moisture and gaseous oxygen to the

Address correspondence to xbzhang@ciac.ac.cn

lithium, thereby limiting the performance of the battery. In response, intensive research has been devoted to the protection of Li anodes by modifying the OE, including constructing a protective film on the Li anode. These methods have proven to protect the Li anode, but only to some extent. Unfortunately, it is difficult to make a suitable protective film on the Li anode because it is too active [6]. Furthermore, the serious decomposition and volatilization of OE and the diffusion of oxygen and other impurities from the cathode are still not resolved [7, 8]. Alternatively, replacing the OE with a solid electrolyte might be a good choice. Generally, solid electrolytes can be classified into two groups: Polymers electrolytes (PE) and inorganic ceramic electrolytes (CE). Interestingly, PEs are flexible and they hold an outstanding wetting ability toward the electrodes. However, the lithium ion conductivity of PEs is poor, and its decomposition at high temperatures becomes exacerbated, especially in the strong oxidizing environment of Li-O$_2$ batteries [9–11]. In sharp contrast, CEs offers a satisfactory lithium ion conductivity, a high Young's modulus, an outstanding thermal stability and a high Li$^+$ transfer number [12, 13]. Among CEs, garnet-ceramic electrolytes are very promising for Li-O$_2$ battery because they have a stable contact with Li and oxygen, wide electrochemical window, and high thermal stability [14–16]. However, taking into account the unique semi-open system of Li-O$_2$ batteries and the characteristics of garnet electrolytes, there are two important issues that need to be addressed. First is the unwanted generation of the poor Li$^+$ conductor, lithium carbonate, which is a product of the garnet electrolyte being exposed to the moisture that inevitably exists in Li-O$_2$ batteries [17–19]. The second issue is the large interfacial resistance between the ceramic electrolyte and the electrode due to its rigidity [20–22]. Therefore, for the sake of mutual complementation, it is highly desirable to combine CEs with OEs to form a hybrid electrolyte to be used in Li-O$_2$ batteries.

In this work, as a proof-of-concept experiment, a hybrid electrolyte system, an organic/ceramic/organic electrolyte (OCOE) combination, is proposed and demonstrated. This hybrid electrolyte aims to protect the Li anode in Li-O$_2$ batteries. A robust garnet-ceramic electrolyte Li$_{6.5}$La$_3$Zr$_{1.5}$Ta$_{0.5}$O$_{12}$ (LLZT) with good air

stability is firstly synthesized. Because of the suitable sandwich structure of OCOE configurations and the robust mechanical and chemical properties of CEs, oxygen shuttle and OE decomposition are obviously inhibited, and thus, the corrosion of the Li anode is significantly suppressed and the battery performance is effectively improved.

2 Experiment

2.1 Synthesis of garnet-ceramic electrolyte

LLZT electrolytes with nominal composition of LLZT-x Al$_2$O$_3$ with $x = 0$ wt.%, 1 wt.%, 2 wt.%, 3 wt.%, 4 wt.%, and 5 wt.% were prepared (denoted as LLZT-x A). Briefly, LiOH·H$_2$O (99.99%), La(OH)$_3$ (99.99%), ZrO$_2$ (99.99%), Ta$_2$O$_5$ (99.99%) powders were weighted in stoichiometric ratio, and mixed in a mortar for 2 h to obtain stoichiometry of Li$_{6.5}$La$_3$Zr$_{1.5}$Ta$_{0.5}$O$_{12}$. An excess of 15 wt. % LiOH·H$_2$O was used to compensate for the lithium loss during high-temperature sintering. The resulting mixture was heated at 900 ℃ for 6 h. The obtained mother powders with different amounts of Al$_2$O$_3$ were reground for another 1 h and then cold-pressed into pellets having a diameter of 12 mm at 200 MPa for 5 min. The green pellets were buried under the mother powder and sintered in aluminum crucibles with a cover at 1,150 ℃ for 8 h. The resulting pellets were mechanically polished with P2000 sand papers and stored in an argon-filled glove box (with water and oxygen contents below 0.1 ppm) to prevent any reaction with moisture. To characterize the stability of LLZT against moisture, pellets were exposed to ambient air (50% relative humidity) at 30 ℃ (room temperature, RT).

2.2 Characterizations

The sample phases were examined by powder X-ray diffraction (XRD) measurement on a Bruker D8 Focus Powder X-ray diffractometer with Cu Kα ($\lambda = 0.15405$ nm). The XRD patterns of LLZT-x A were obtained on the smooth surface of the pellets. Scanning electron microscopy (SEM) was performed with a field emission scanning electron microanalyzer (Hitachi S4800), operating at an accelerating voltage of 10 kV. For observing the cross-section microstructure of LLZT-x A, the pellets

were broken off. X-ray photoelectron spectroscopy (XPS) analyses were carried out on an ESCALAB MKII X-ray photoelectron spectrometer. The Raman spectrum of the pellets was collected using a micro-Raman spectrometer (Renishaw) with a 532 nm wavelength laser. The intensity curves were normalized by the corresponding maximum values. Ionic conductivities of the pellets were determined using a BioLogic VMP3 electrochemical workstation for frequencies ranging from 100 Hz to 7 MHz at an AC amplitude of 10 mV. The Ag ink was painted on both sides of the pellets and dried at 175 °C for 2 h. The plots were analyzed using the Zview software. The relative density was calculated geometrically. ^{1}H NMR spectra were recorded by a Bruker Avance II 400 spectrometer. For the ^{1}H NMR test, after first being fully charged, the fully rinsed and dried glass fiber (GF) paper adjacent to the cathode was extracted with D_2O. The stability of LLZT towards O_2^- was tested using KO_2. A 20 μL KO_2/OE solution (0.05 M) was dropped on the surface of LLZT-2 A and was allowed to dry in an argon-filled glove box for several days at room temperature.

2.3 The assembly of the Li-O$_2$ battery

To prepare the cathode, 80 wt.% Super P and 20 wt.% PVDF was mixed in N-methyl-2-pyrrolidone. Then, the slurry was painted on carbon paper using Super P loading of around 0.5 mg·cm^{-2}. The cathode was dried in a vacuum oven at 80 °C. Assembly of the 2032 type Li-O$_2$ batteries was performed in an argon filled glove box with lithium foil as the anode and either OCOE or OE being immersed in GF as the electrolyte. The OE contained 1 M lithium trifluoro-methanesulfonate (LiCF$_3$SO$_3$) in tetraethylene glycol dimethyl ether (TEGDME). TEGDME was dried with activated molecular sieves (4 Å type) for one month until the water content was below 10 ppm. The structure of batteries is illustrated in Fig. S1 in the Electronic Supplementary Material (ESM). In order to ensure that oxygen can be fully diffused in the cathode, foam nickel was placed on the cathode. The Li-O$_2$ batteries were tested at 60 °C on a LAND CT2001A multi-channel battery testing system. The rate of the Li anode corrosion was slow when the battery was tested at room temperature. A temperature of 60 °C was then chosen for two reasons. First, tests carried out at 60 °C would

speed up the experimental process and highlight the effect. Second, batteries have to sometimes run at high temperatures in many applications [23, 24].

3   Results and discussion

To identify the phase and purity of the as-obtained pellets, XRD tests were carried out. As shown in Fig. 1 above and Fig. S2 in the ESM, the powder and all the pellets of LLZT crystallized in the cubic garnet phase, which is consistent with other reports [25, 26]. Some minor peaks characteristic of LiAlO$_2$ appeared at around 23 degrees when Al$_2$O$_3$ was added in the sintering process [27]. No peaks related to Al$_2$O$_3$ were observed, indicating that the amount of Al$_2$O$_3$ had no effect on the major phase (cubic garnet phase) of the pellets. Because ionic conductivity is an important parameter of CEs, the ionic conductivity of LLZT-x A was tested to observe the effect of Al$_2$O$_3$ on it. The impedance plots of the pellets show the effect of Al$_2$O$_3$ on ionic conductivity (Fig. 1(b) and Fig. S3 in the ESM). The LLZT-0 A exhibited the highest ionic conductivity even if it had a lower density than the Al$_2$O$_3$ added pellets. LLZT-2 A not only had the highest density but also the highest ionic conductivity among the Al$_2$O$_3$ added pellets (Table S1 in the ESM). It can be found that density of the samples increases at first but then then decreases steadily with an increasing amount of Al$_2$O$_3$, and the optimum value was obtained when the addition amount was 2 wt.% (Fig. 1(c)). To further investigate the effect of Al$_2$O$_3$ on the density of pellets, SEM was used to observe their morphology. In the absence of Al$_2$O$_3$, there were many holes among the grains and the grain size was uneven. In sharp contrast, when Al$_2$O$_3$ was added, the grain size exhibited an increasing trend, and the grain size became more and more uniform. It is noteworthy that holes among the grains disappeared, indicating that Al$_2$O$_3$ played a key role in improving the density of LLZT. However, when the Al$_2$O$_3$ content exceeded 2 wt.%, the holes appeared again. This indicates that excess Al$_2$O$_3$ was ineffectual in significantly improving the density under this sintering schedule. In order to analyze the reason of the increasing density mentioned above, EDX mapping was used. As shown in Fig. S4 in the ESM, the Al element was mainly concentrated at the
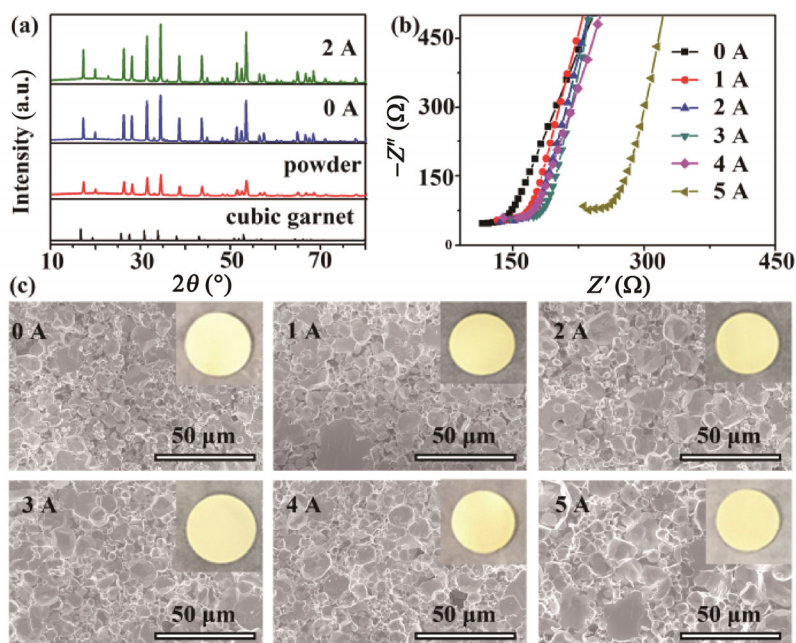
Figure 1 (a) XRD patterns of LLZT with different amounts of Al_2O_3. The diffraction patterns of cubic garnet refer to PDF # 80-0457. (b) Impedance plots of LLZT with different amounts of Al_2O_3. (c) Cross-section SEM images of LLZT-x A. Insets are digital pictures of the corresponding pellets.

grain boundaries, which can improve the connection among the grains and promote the densification of the sample [28]. However, the ionic conductivity of the Al-contained species at the grain boundaries was lower than that of the cubic garnet grains, which may result in a slight decrease in ionic conductivity of pellets contain Al_2O_3. All the samples were yellow in color, but the shade of LLZT-0 A was lighter. As was expected, after adding Al_2O_3, the sample color became dark yellow, which was consistent with the microstructure. Therefore, LLZT-0 A and LLZT-2 A were picked to be tested as examples.

Inspired by the successful improvement of the density, its effect on the air stability of the pellets was investigated. For this purpose, Raman and XPS studies of the pellets, following exposure in ambient air, were performed to observe whether LLZT-2 A would generate less lithium carbonate than LLZT-0 A. As shown in Fig. 2(a), Li_2CO_3 was detected on both of the samples and the amount of Li_2CO_3 increased as time went on. Nevertheless, it is worth noting that the amount of Li_2CO_3 in LLZT-2 A was much less than in LLZT-0 A, regardless of how long it was exposed to air, judged by the peaks of Li_2CO_3 on the Raman spectrums. This result was further proven by the XPS results. Figure 2(b) describes

the typical C 1s spectra of the pellets. Two peaks located at 289 and 285 eV can be assigned to Li_2CO_3 and absorbed carbonate, respectively. Compared with LLZT-0 A, the C 1s peak of Li_2CO_3 for LLZT-2 A is less strong, indicating that the amount of Li_2CO_3 in LLZT-2 A is less than in LLZT-0 A. A compact pellet could lower the generation rate of Li_2CO_3 because Li_2CO_3 tends to appear at grain boundaries and holes. Therefore, the air stability of LLZT can be greatly improved with an increase in density. These results indicate that the robust LLZT-2 A ceramic electrolyte is sufficiently stable. These results are encouraging for further studies regarding Li-O_2 batteries.

With the above improvement in mind, a distinctive hybrid electrolyte system with an OCOE architecture that combines the strengths of OE and LLZT-2 A, was introduced to Li-O_2 batteries. The first discharge-charge test was performed to verify the reversibility of the batteries. At a current density of 200 mA·g^{-1}, the Li-O_2 battery with OE exhibited a lower capacity than that with OCOE (Fig. 3(a)). Even if the current density was reduced to 100 mA·g^{-1}, the discharge capacity of Li-O_2 battery with OE would still be less than that with OCOE. Surprisingly, the Li-O_2 battery with OCOE electrolyte could be reversibly discharged and charged.
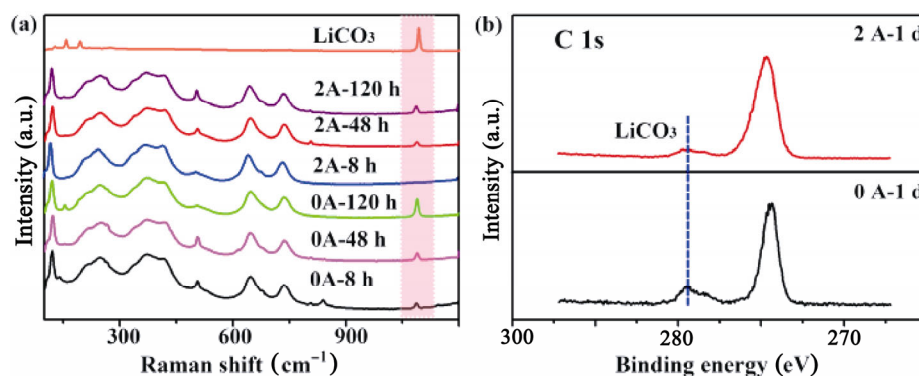
Figure 2 (a) Raman spectrums of LLZT-0 A and LLZT-2 A before and after been exposed to ambient air for different durations (8 to 120 h). (b) C 1s spectrum of LLZT-0 A and LLZT-2 A after been exposed to ambient air for 1 day.

However, the battery with the OE electrolyte was not able to be charged fully, even if the current was set to a smaller value. In order to explore the causes behind this phenomenon, SEM tests were carried out to observe the morphology of lithium anode after being charged. Prior to the first charge process, the surface of the pristine lithium anode was very smooth, but had changed dramatically after (Fig. S5 in the ESM). As can be seen from Fig. 3(b), the morphology of the lithium anodes from the charged Li-O$_2$ batteries with OE and OCOE is completely different. Compared with a pristine lithium anode, the surface of the lithium anode in the OE batteries became rougher and many observable cracks developed. This indicates that the corrosion of the lithium anode resulted in irreversibility of the Li-O$_2$ batteries that used OE. In sharp contrast, the lithium anode in the Li-O$_2$ with OCOE was still smooth, despite being covered by some particles. This suggests that the OCOE electrolyte successfully suppressed parasitic reactions on the Li anode. Although the garnet electrolyte has strong antioxidant capacities, its stability in real Li-O$_2$ batteries still needs to be confirmed. To investigate the stability of LLZT in Li-O$_2$ batteries, XRD patterns of LLZT-2A facing cathode after being charged to 4.5 V are shown in Fig. 3(c). Remarkably, the absence of any impurity phases suggests that the LLZT-2 A is sufficiently stable in Li-O$_2$ batteries having strong oxidizing environment. In addition, to further examine the stability of LLZT-2 A towards O$_2^-$, the chemical reaction between LLZT-2 A and KO$_2$ was investigated by XRD. No change was observed except for the peaks of the vacuum sample cell (Fig. S6 in the ESM). [29]. Furthermore, the phase

and morphology of discharged products in Li-O$_2$ batteries with OE or OCOE were studied. Toroid-like Li$_2$O$_2$ was formed and decomposed reversibly in both batteries (Fig. 3(d) and Fig. S7 in the ESM), indicating that the introduction of OCOE does not affect the electrochemical reaction of Li-O$_2$ batteries [30]. It is worth noting that massive byproducts adhered to the cathode after the Li-O$_2$ batteries with OE were charged. On the other hand, the morphology of the cathode remained well in the Li-O$_2$ batteries with OCOE. This also demonstrates that the decomposition of OE is suppressed in Li-O$_2$ batteries with OCOE [31].

According to the above study, OCOE with LLZT of different densities would have an impact on performance of Li-O$_2$ batteries. As shown in Fig. 4(a), compared with the batteries with LLZT-0 A, the batteries with LLZT-2 A exhibit better performance. The cycling life of the Li-O$_2$ batteries with LLZA-2 A is much longer than that with LLZA-0 A, which is explained by the fact that LLZT-2 A is more effective in keeping lithium away from moisture and oxygen. Encouraged by this phenomenon, the cycling performance of Li-O$_2$ battery with OE and OCOE containing LLZT-2 A was tested. Li-O$_2$ batteries with the OCOE electrolyte could be cycled up to 43 times. In sharp contrast, Li-O$_2$ batteries with the OE electrolyte only ran for 14 cycles (Figs. 4(b) and 4(c) and Fig. S8 in the ESM). This clear improvement in cycling performance is believed to stem from the effective suppression of Li anode corrosion through the alleviation of OE decomposition. For further verification, the parasitic reaction of OE was examined by ^{1}H NMR spectra. The results show that the amount of organic electrolyte decomposition products (CH$_3$CO$_2$Li and
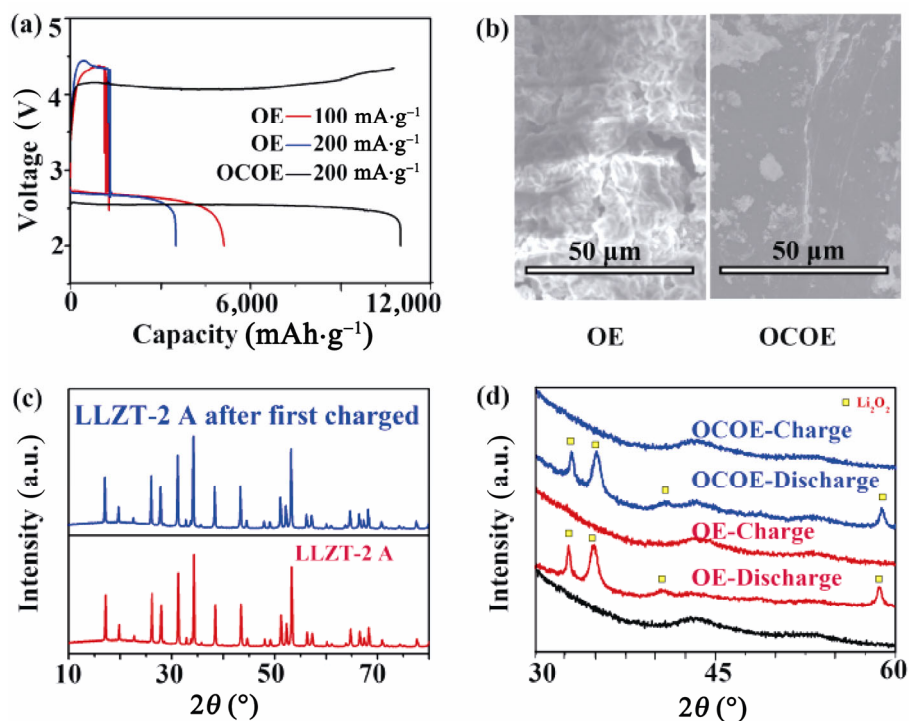
Figure 3 (a) First discharge-charge curves of Li-O$_2$ battery with OE or OCOE containing LLZT-2 A (2–4.5 V). (b) SEM images of Li anode from the charged Li-O$_2$ battery with OE or OCOE. (c) XRD patterns of LLZT-2 A sintered before and after first charged. (d) XRD patterns of cathode in the Li-O$_2$ battery with OE or OCOE at pristine, first discharged and first charged states.
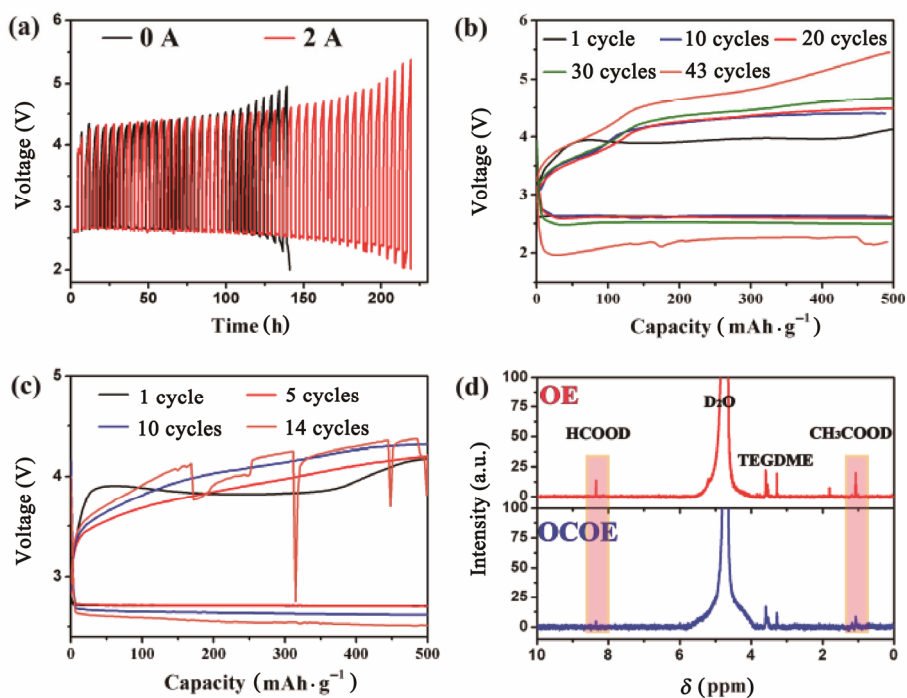
Figure 4 (a) The cycle life of Li-O$_2$ batteries with OCOE containing LLZT-0 A or LLZT-2 A (current densities: 200 mA·g^{-1}). (b) The cycle performance of Li-O$_2$ battery with OCOE containing LLZT-2 A (current densities: 200 mA·g^{-1}). (c) The cycle performance of Li-O$_2$ battery with OE (current densities: 200 mA·g^{-1}). (d) ^{1}H NMR spectra of GF taken from Li-O$_2$ batteries with OE or OCOE containing LLZT-2 A after the first cycle.

HCO₂Li) in the OCOE electrolyte was much less than that in the OE electrolyte (Fig. 4(d)) [32]. The amount of LiOH on the Li anode can be used as a standard for the degree of lithium corrosion [33]. After the first charge, XRD diffraction peaks of LiOH on the Li anode of the Li-O$_2$ batteries with either OE or OCOE were detectable (Fig. S9 in the ESM). Importantly, the peaks of LiOH are much weaker for the Li anode in the Li-O$_2$ battery with OCOE, indicating that the decomposition of OE is significantly suppressed in Li-O$_2$ batteries with OCOE.

According to the above analysis, the excellent performance obtained is due to multiple advantages of OCOE, as illustrated in Fig. 5. First, the inevitable crossover of O$_2$ is stopped using the dense garnet electrolyte, which reduces the anodic side reaction of lithium. Second, an image description of the electric potential profile across the electrolyte is given. Thanks to the introduction of the garnet electrolyte, the potential difference resisted by OE is reduced. Consequently, the decomposition of the OE is suppressed resulting in the Li anode being protected. Therefore, we believe that the method of using OCOE is a viable strategy for Li anode protection in Li–O$_2$ batteries.
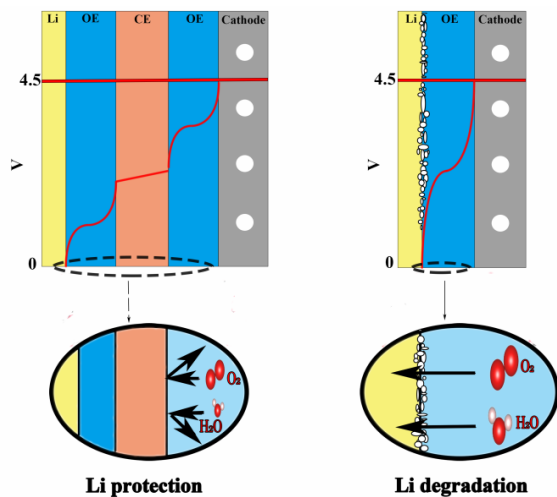
Figure 5 A schematic illustration of protection mechanism of OCOE. Red curves indicate the electric potential profile across the OCOE.

4 Conclusions

In summary, to achieve a stable Li-O$_2$ battery, a hybrid electrolyte system with an OCOE architecture was proposed to alleviate the corrosion of the lithium anode.

Unexpectedly, as a proof-of-concept application, when the OCOE was used as a novel electrolyte system for Li-O$_2$ batteries, a significantly optimized cycling performance was obtained compared with batteries with an OE electrolyte. We believe that this Li anode protection strategy provides a new way of thinking as well as excitement for more researches concerning the protection of Li anodes in Li-O$_2$ batteries and other ultrahigh density Li-metal batteries, such as Li/LiMn$_2$O$_4$, Li/LiCoO$_2$ and Li/Br.

References

[1] Bruce, P. G.; Freunberger, S. A.; Hardwick, L. J.; Tarascon, J. M. Li-O$_2$ and Li-S batteries with high energy storage. *Nat. Mater.* **2012**, *11*, 19–29.

[2] Chu, S.; Cui, Y.; Liu, N. The path towards sustainable energy. *Nat. Mater.* **2017**, *16*, 16–22.

[3] Goodenough, J B. Changing outlook for rechargeable batteries. *ACS Catal.* **2017**, *7*, 1132–1135.

[4] Xu, J. J.; Liu, Q. C.; Yu, Y.; Wang, J.; Yan, J. M.; Zhang, X. B. *In situ* construction of stable tissue-directed/reinforced bifunctional separator/protection film on lithium anode for lithium-oxygen batteries. *Adv. Mater.* **2017**, *29*, 1606552.

[5] Freunberger, S. A.; Chen, Y. H.; Drewett, N. E.; Hardwick, L. J.; Bardé, F.; Bruce, P. G. The lithium-oxygen battery with ether-based electrolytes. *Angew. Chem., Int. Ed.* **2011**, *50*, 8609–8613.

[6] Kim, B. G.; Kim, J. S.; Min, J.; Lee, Y. H.; Choi, J. H.; Jang, M. C.; Freunberger, S. A.; Choi, J. W. A moisture- and oxygen-impermeable separator for aprotic Li-O$_2$ batteries. *Adv. Funct. Mater.* **2016**, *26*, 1747–1756.

[7] Liu, B.; Xu, W.; Yan, P. F.; Kim, S. T.; Engelhard, M. H.; Sun, X. L.; Mei, D. H.; Cho, J.; Wang, C. M.; Zhang, J. G.

Stabilization of Li metal anode in DMSO-based electrolytes via optimization of salt-solvent coordination for Li-O$_2$ batteries. *Adv. Energy Mater.* **2017**, *7*, 1602605.

[8]   Liu, Q. C.; Xu, J. J.; Yuan, S.; Chang, Z. W.; Xu, D.; Yin, Y. B.; Li, L.; Zhong, H. X.; Jiang, Y. S.; Yan, J. M.; Zhang, X. B. Artificial protection film on lithium metal anode toward long-cycle-life lithium-oxygen batteries. *Adv. Mater.* **2015**, *27*, 5241–5247.

[9]   Balaish, M.; Peled, E.; Golodnitsky, D.; Ein-Eli, Y. Liquid-free lithium-oxygen batteries. *Angew. Chem., Int. Ed.* **2015**, *54*, 436–440.

[10] Elia, G. A.; Hassoun, J. A polymer lithium-oxygen battery. *Sci. Rep.* **2015**, *5*, 12307.

[11] Wu, C.; Liao, C. B.; Li, T. R.; Shi, Y. Q.; Luo, J. S.; Li, L.; Yang, J. A polymer lithium–oxygen battery based on semi-polymeric conducting ionomers as the polymer electrolyte. *J. Mater. Chem. A* **2016**, *4*, 15189–15196.

[12] Han, F. D.; Zhu, Y. Z.; He, X. F.; Mo, Y. F.; Wang, C. S. Electrochemical stability of Li$_{10}$GeP$_2$S$_{12}$ and Li$_7$La$_3$Zr$_2$O$_{12}$ solid electrolytes. *Adv. Energy Mater.* **2016**, *6*, 1501590.

[13] Janek, J.; Zeier, W. G. A solid future for battery development. *Nat. Energy* **2016**, *1*, 16141.

[14] Li, F. J.; Kitaura, H.; Zhou, H. S. The pursuit of rechargeable solid-state Li-air batteries. *Energy Environ. Sci.* **2013**, *6*, 2302–2311.

[15] Li, Y. Q.; Cao, Y.; Guo, X. X. Influence of lithium oxide additives on densification and ionic conductivity of garnet-type Li$_{6.75}$La$_3$Zr$_{1.75}$Ta$_{0.25}$O$_{12}$ solid electrolytes. *Solid State Ionics* **2013**, *253*, 76–80.

[16] Ma, C.; Cheng, Y. Q.; Yin, K. B.; Luo, J.; Sharafi, A.; Sakamoto, J.; Li, J. C.; More, K. L.; Dudney, N. J.; Chi, M. F. Interfacial stability of Li metal-solid electrolyte elucidated via *in situ* electron microscopy. *Nano Lett.* **2016**, *16*, 7030–7036.

[17] Sharafi, A.; Yu, S.; Naguib, M.; Lee, M.; Ma, C.; Meyer, H. M.; Nanda, J.; Chi, M.; Siegel, D. J.; Sakamoto, J. Impact of air exposure and surface chemistry on Li–Li$_7$La$_3$Zr$_2$O$_{12}$ interfacial resistance. *J. Mater. Chem. A* **2017**, *5*, 13475–13487.

[18] Xia, W. H.; Xu, B. N.; Duan, H. N.; Guo, Y. P.; Kang, H. M.; Li, H.; Liu, H. Z. Ionic conductivity and air stability of Al-doped Li$_7$La$_3$Zr$_2$O$_{12}$ sintered in alumina and Pt crucibles. *ACS Appl. Mater. Interfaces* **2016**, *8*, 5335–5342.

[19] Xia, W. H.; Xu, B. Y.; Duan, H. N.; Tang, X. Y.; Guo, Y. P.; Kang, H. M.; Li, H.; Liu, H. Z. Reaction mechanisms of lithium garnet pellets in ambient air: The effect of humidity and CO$_2$. *J. Am. Ceram. Soc.* **2017**, *100*, 2832–2839.

[20] van den Broek, J.; Afyon, S.; Rupp, J. L. M. Interface-engineered all-solid-state Li-ion batteries based on garnet-type fast Li$^+$ conductors. *Adv. Energy Mater.* **2016**, *6*, 1600736.

[21] Fu, K.; Gong, Y. H.; Hitz, G. T.; McOwen, D. W.; Li, Y. J.; Xu, S. M.; Wen, Y.; Zhang, L.; Wang, C. W.; Pastel, G. et al.

Three-dimensional bilayer garnet solid electrolyte based high energy density lithium metal-sulfur batteries. *Energy Environ. Sci.* **2017**, *10*, 1568–1575.

[22] Wang, C. W.; Gong, Y. H.; Liu, B. Y.; Fu, K.; Yao, Y. G.; Hitz, E.; Li, Y. J.; Dai, J. Q.; Xu, S. M.; Luo, W. et al. Conformal, nanoscale ZnO surface modification of garnet-based solid-state electrolyte for lithium metal anodes. *Nano Lett.* **2017**, *17*, 565–571.

[23] Rodrigues, M. T. F.; Babu, G.; Gullapalli, H.; Kalaga, K.; Sayed, F. N.; Kato, K.; Joyner, J.; Ajayan, P. M. A materials perspective on Li-ion batteries at extreme temperatures. *Nat. Energy* **2017**, *2*, 17108.

[24] Yi, J.; Liu, Y.; Qiao, Y.; He, P.; Zhou, H. S. Boosting the cycle life of Li–O$_2$ batteries at elevated temperature by employing a hybrid polymer–ceramic solid electrolyte. *ACS Energy Lett.* **2017**, *2*, 1378–1384.

[25] Murugan, R.; Thangadurai, V.; Weppner, W. Fast lithium ion conduction in garnet-type Li$_7$La$_3$Zr$_2$O$_{12}$. *Angew. Chem., Int. Ed.* **2007**, *46*, 7778–7781.

[26] Afyon, S.; Krumeich, F.; Rupp, J. L. M. A shortcut to garnet-type fast Li-ion conductors for all-solid state batteries. *J. Mater. Chem. A* **2015**, *3*, 18636.

[27] Liu, K.; Ma, J. T.; Wang, C. A. Excess lithium salt functions more than compensating for lithium loss when synthesizing Li$_{6.5}$La$_3$Zr$_{1.75}$Ta$_{1.5}$O$_{12}$ in alumina crucible. *J. Power Sources* **2014**, *260*, 109–114.

[28] Li, Y. T.; Han, J. T.; Wang, C. A.; Xie, H.; Goodenough, J. B. Optimizing Li$^+$ conductivity in a garnet framework. *J. Mater. Chem.* **2012**, *22*, 15357–15361.

[29] Xu, B. Y.; Duan, H. N.; Liu, H. Z.; Wang, C. A.; Zhong, S. W. Stabilization of garnet/liquid electrolyte interface using superbase additives for hybrid Li batteries. *ACS Appl. Mater. Interfaces* **2017**, *9*, 21077–21082.

[30] Zhou, B.; Guo, L. M.; Zhang, Y. T.; Wang, J. W.; Ma, L. P.; Zhang, W. H.; Fu, Z. W.; Peng, Z. Q. A high-performance Li-O$_2$ battery with a strongly solvating hexamethylphosphoramide electrolyte and a LiPON-protected lithium anode. *Adv. Mater.* **2017**, *29*, 1701568.

[31] Xu, J. J.; Chang, Z. W.; Yin, Y. B.; Zhang, X. B. Nanoengineered ultralight and robust all-metal cathode for high-capacity, stable lithium-oxygen batteries. *ACS Cent. Sci.* **2017**, *3*, 598–604.

[32] Xu, J. J.; Wang, Z. L.; Xu, D.; Meng, F. Z.; Zhang, X. B. 3D ordered macroporous LaFeO$_3$ as efficient electrocatalyst for Li–O$_2$ batteries with enhanced rate capability and cyclic performance. *Energy Environ. Sci.* **2014**, *7*, 2213–2219.

[33] Wu, S. C.; Qiao, Y.; Yang, S. X.; Ishida, M.; He, P.; Zhou, H. S. Organic hydrogen peroxide-driven low charge potentials for high-performance lithium-oxygen batteries with carbon cathodes. *Nat. Commun.* **2017**, *8*, 15607.